IEEE Access
Multidisciplinary | Rapid Review | Open Access Journal

Received 6 August 2022, accepted 20 October 2022, date of publication 3 November 2022, date of current version 14 November 2022.

Digital Object Identifier 10.1109/ACCESS.2022.3219201

RESEARCH ARTICLE

Fusion of Signal Processing Techniques to Design Current and Voltage Features Based Protection Scheme for Utility Grid With Renewable Energy Penetration

ABHISHEK GUPTA[1], RAMESH KUMAR PACHAR[1], OM PRAKASH MAHELA[2], (Senior Member, IEEE), AND BASEEM KHAN[3], (Senior Member, IEEE)

[1]Department of Electrical Engineering, Swami Keshvanand Institute of Technology, Management and Gramothan, Jaipur 302017, India
[2]Power System Planning Division, Rajasthan Rajya Vidyut Prasaran Nigam Ltd., Jaipur 302005, India
[3]Department of Electrical Engineering, Hawassa University, Hawassa 05, Ethiopia

Corresponding author: Baseem Khan (baseem.khan04@gmail.com)

ABSTRACT This paper used fusion of Hilbert transform (HT), Stockwell transform (ST) and Alienation coefficient to design a protection scheme for utility network with high concentration of renewable energy (RE) generation. A hybrid fault detection index (HFDI) is designed which detects the fault events utilizing the features extracted from both current and voltage signals. Peak magnitude of HFDI is compared with a threshold magnitude (HTM) to detect fault events and discriminate such events from operational events. Faults are classified based on faulty phase numbers and a hybrid ground fault index (HGFI). Zero sequence voltage and zero sequence current are processed by application of ST to compute HGFI which effectively detects presence of ground during fault event. Performance of protection scheme is validated using utility grid of IEEE-13 bus test system where 50% RE penetration is used. Further, performance is also tested to detect faults incident on a practical utility network with RE penetration of 57%. Performance of algorithm is evaluated to recognize different fault events and operational events. Protection scheme is effectively tested to detect faults with high noise levels of 20 dB SNR (signal to noise ratio). Proposed protection scheme perform better compared to Alienation coefficient based protection scheme reported in literature.

INDEX TERMS Alienation coefficient, fault event, Hilbert transform, protection scheme, Stockwell transform, utility grid.

ABBREVIATIONS

ABCF	Three phase fault
ABCGF	Three phase fault involving ground
ABF	Phase-A and phase-B fault
ABGF	Phase-A and phase-B fault with involvement of ground
AGF	Phase-A to ground fault
AC	Alternating current
A-index	Alienation index
CORC	Correlation coefficient
COVF	Co-variance factor
COVFZI	Zero sequence current co-variance factor
DG	Distributed generator
DT	Distribution transformer
DTRF	Distribution transformer
EMD	Empirical Mode Decomposition
EV	Electric vehicle
GWT	Gabor–Wigner transform
HCI	Hilbert transform current index
HFDI	Hybrid fault detection index
HGFI	Hybrid ground fault index

The associate editor coordinating the review of this manuscript and approving it for publication was Ali Raza.

HH-index	Hybrid Hilbert index
HPSL	Hybrid protection scheme location node
HS-index	Hybrid Stockwell index
HT	Hilbert transform
HTM	Threshold magnitude
HVI	Hilbert transform voltage index
HWF	Hybrid weight factor
HZT	Hybrid zero sequence threshold
IEEE	Institute of Electrical and Electronics Engineers
KF	Kalman filter
MG	Micro-grid
MM	Mathematical Morphology
MODWT	Maximal Overlap Discrete Wavelet Transform
NFP	Number of faulty phases
PCC	Pearson Correlation Coefficient
PV	Photovoltaic
RE	Renewable energy
SNR	Signal to noise ratio
SPP	Solar power plant
SS	Sub-station
SST	Sub-station transformer
ST	Stockwell transform
SVM	Support vector machine
TTT	Time–Time transform
UGTRF	Utility grid transformer
WPP	Wind power plant
WT	Wavelet Transform
WTRF	Wind transformer
ZWF	Zero sequence weight factor

I. INTRODUCTION

The micro-grids (MG) and distributed generators are recent movements in the energy sector. Use of fossil fuels is continuously decreasing and renewable sources are considered as an effective, optimal and efficient way for future energy demand. Wind turbines and solar photovoltaic (PV) systems are most prominent sources of energy which are interfaced to the utility grids in the form of distributed generators (DG) [1]. DGs inject real and reactive power into the network of utility grid. This helps to reduce loss, increase grid resilience, and mitigate voltage sag during period of fault events. Apart from these benefits, high RE integration levels causes challenges in terms of protection due to power reversal in feeders, harmonic injections by converters, and fast ramp up/down rate due to generation uncertainty [2]. Signal processing techniques like Hilbert Transform (HT), Kalman filter (KF), Stockwell transform (ST), Gabor–Wigner transform (GWT), Mathematical Morphology (MM), Wavelet Transform (WT), Time–Time transform (TTT), Alienation coefficient, and Empirical Mode Decomposition (EMD) can effectively be used to design fault protection schemes of utility grids with RE integration [3]. A fault detection technique derived by data fault location using Gaussian process regression applied to a smart AC micro-grid is designed in [4]. In [5], authors introduced a detailed study investigate the impacts of DG integration into the grids on voltage profile, fault detection schemes and fault current levels. In [6], authors designed differential scheme of fault detection and classification using Maximal Overlap Discrete Wavelet Transform (MODWT). This protection scheme effectively applied to the micro-grid with DG sources. In [7], authors presented a study on sensor fault detection and isolation scheme and applied the same to detect fault events incident on interconnected smart network of power systems with high share of RE and feeding power electric vehicle (EV) charging stations. In [8], authors applied fuzzy system to design a protection approach for detection and classification of the short circuit fault incident on transmission line used for integration of wind power plant (WPP) to network of utility grid. A Pearson Correlation Coefficient (PCC) and support vector machine (SVM) based algorithm to detect high impedance arcing faults incident on micro-grids interfaced with DGs is introduced in [9]. Protection scheme is fast and detect faults with high accuracy. In [10], authors designed a protection approach for low impedance faults incident on micro-grids using flow direction of active power, voltage sag magnitude and current magnitude. Approach is effective to provide protection against low impedance faults of all types incident on micro-grids of every topology, configuration and every mode of operation.

Detailed review and analysis of above discussed protection techniques indicates that fusion of signal processing techniques to extract features of both current and voltage signals can be used for improvement in performance of the protection schemes with high RE concentration. This is identified as fault detection research gaps and considered in this study. Key research contributions of this paper are detailed below:

- Fusion of Signal Processing Techniques such as HT, ST, and alienation coefficient is used to design a protection scheme using features of both current and voltage signals which is effective to detect fault events incident on network of Utility with RE concentration.
- A HFDI is designed which is effective for detection of different fault events with RE presence. This is performed by comparing peak magnitude of HFDI with a threshold value.
- A HGFI is formulated by processing the zero sequence voltage and zero sequence current applying the ST to detect presence of ground with a fault. Faults are classified considering faulty phase numbers and HGFI.
- Performance of designed protection scheme is effectively validated using utility grid of IEEE-13 bus test system where 50% RE penetration is used. Further, performance is also tested to detect faults incident on a practical distribution network with RE concentration of 57%.
- Algorithm works well for various case studies of fault events and discriminates faults from operational events. Protection scheme is also effective to detect faults with high noise levels of 20dB SNR.

- Protection scheme is superior compared to Alienation coefficient based protection scheme reported in literature.

The structure of this paper includes nine sections. Review of existing literature, research gaps and contribution in the research field are detailed in Section I. Test utility network interfaced with RE generators and implemented for validation of study is elaborated in Section II. Designed protection algorithm is described and illustrated in Section III. Results of simulation to describe fault detection are included in Section IV. Validation of protection algorithm on different cases of study are elaborated in Section V. Discrimination of fault events from the operational events is described using simulation results in Section VI. Testing of protection scheme on the practical utility grid is detailed in Section VII. Performance comparative analysis is described in Section VIII. Research conclusions are included in Section IX.

II. TEST UTILITY GRID INTERFACED WITH RE GENERATORS

Test utility grid is realized by integration of a solar power plant (SPP) rated at $1MW$ capacity and a WPP rated at a capacity of 1.5 MW to IEEE-13 nodes test system as described in Fig. 1. Test utility grid is rated at $5MVA$ and operated $60Hz$ frequency, voltages of 0.48 kV & 4.16 kV. All nodes are rated at 4.16 kV except node 634 which is operated at 0.48 kV. Hence, RE penetration level of 50% is used in this study. Utility grid transformer (UGTRF) is used to integrate the test network to the large area utility grid which is operated at $115kV$ [11]. SPP rated at $1MW$ is interfaced on 680 node with the help of STRF transformer and modelled using the parameters reported in [12]. WPP rated at 1.5 MW is integrated on node 680 with the help of WTRF transformer. WPP is modelled using parameters reported in [13]. Node 671 of test utility grid is taken as dault incidence node. Current and voltage are monitored and recorded at node 650 of test grid which is designated as hybrid protection scheme location (HPSL) point. Distribution transformer (DTRF) is used to operate node 634 at 0.48 kV and all other nodes are operated at 4.16 kV. Transformer details are provided in Table 1. Load data, capacitor data and feeder data available in [14] are utilized in this study.

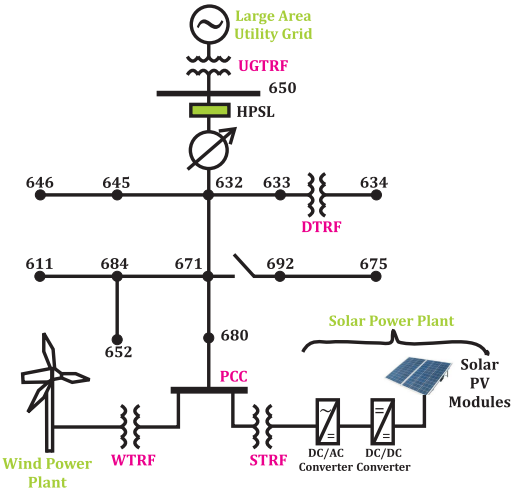

FIGURE 1. Test utility grid network interfaced with RE generators.

III. PROPOSED HYBRID PROTECTION SCHEME FOR UTILITY GRID WITH RE CONCENTRATION

Proposed algorithm for fault detection and classification using fusion of signal processing methods to design a protection scheme for utility grid with RE concentration is enumerated in this section.

A. DETECTION OF FAULT EVENTS

A hybrid fault detection index (HFDI) is designed to detect the fault events which is illustrated in Fig.2. It is based on the processing of both current and voltage waveform using ST, HT and alienation coefficient. HFDI, hybrid Hilbert index (HH-index), hybrid Stockwell index (HS-index) and alienation index (A-index) are detailed in this section.

1) HYBRID HILBERT INDEX

The hybrid Hilbert index (HH-index) is formulated by processing both current and voltage signals by application of HT with sampling frequency of 3.84 kHz. Current ($i(t)$) is processed by application of HT for computation of absolute values of output matrix which is designated as HT current index (HCI) [15].

$$HCI = abs\left(\frac{1}{\pi}PV\int_{-\infty}^{+\infty}\frac{i(\tau)}{t-\tau}d\tau\right) \tag{1}$$

Here, PV, t, and τ indicate the Cauchy's principle value integral, time, and time period respectively. Voltage ($v(t)$) is processed using HT as detailed below to compute absolute values of output matrix which is considered as HT voltage index (HVI) [15].

$$HVI = abs\left(\frac{1}{\pi}PV\int_{-\infty}^{+\infty}\frac{v(\tau)}{t-\tau}d\tau\right) \tag{2}$$

HH-index is computed by multiplication of HCI and HVI as detailed below:-

$$HHindex = HVI \times HCI \tag{3}$$

High magnitude during fault period and least effect of noise are main advantages of HH-index.

2) HYBRID STOCKWELL INDEX

Process the current signal ($i(t)$) using ST considering 3.84 kHz sampling frequency to compute output matrix with absolute values (STAMI) as detailed below [16], [17].

$$STAMI(\tau,f) = \left(\int_{-\infty}^{+\infty} i(t)\frac{|f|}{\sqrt{2\pi}}e^{-\frac{f^2(\tau-t)^2}{2}}e^{-j2\pi ft}dt\right) \tag{4}$$

Here, t, f, and $g(t)$ indicate spectral localization time, Fourier frequency, and Gaussian window function respectively.

TABLE 1. Transformer parameters.

Transformer	MVA	kV FW	kV SW	First Winding		Second Winding	
				R(Ω)	X(Ω)	R(Ω)	X(Ω)
UGTRF	10	115.00	4.16	29.090	211.60	0.1145	0.8308
DTRF	5	4.16	0.48	0.3807	2.7689	0.0511	0.0042
STRF	1	4.16	0.260	0.1730	195.70	0.0008	0.7645
WTRF	5	4.16	0.575	0.3807	2.7688	0.0510	0.0042

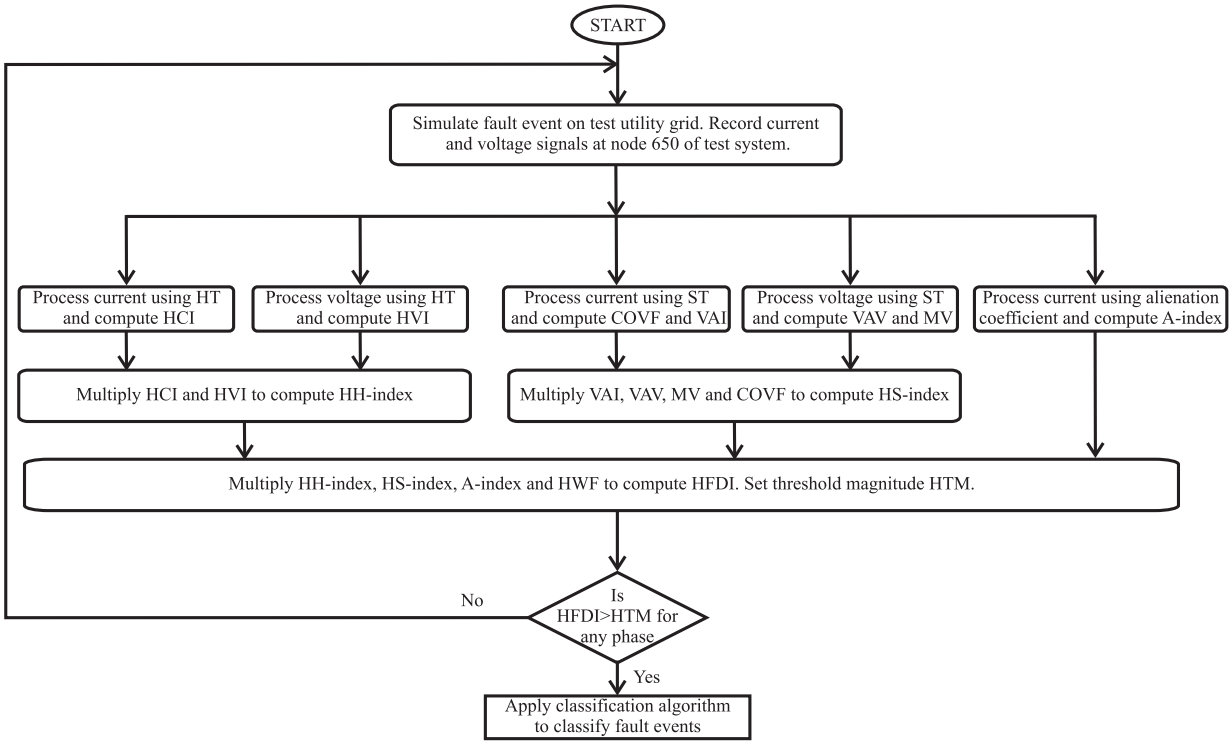

FIGURE 2. Fault detection algorithm.

Compute summation of every element of a column of the matrix STAMI and then take co-variance for computing co-variance factor (COVF) as described below.

$$COVF = cov(sum(STAMI)) \tag{5}$$

Compute summation of all elements in a column of the matrix STAMI with the application below detailed relation.

$$VAI = sum(STAMI) \tag{6}$$

Process the voltage signal ($v(t)$) using ST with considering 3.84 kHz sampling frequency and output matrix with absolute values (STAMV) is computed as detailed below [16], [17].

$$STAMV(\tau, f) = \left(\int_{-\infty}^{+\infty} v(t) \frac{|f|}{\sqrt{2\pi}} e^{-\frac{f^2(\tau-t)^2}{2}} e^{-j2\pi ft} dt \right) \tag{7}$$

Compute summation of all elements in a column of the matrix STAMV applying the below detailed relation.

$$VAV = sum(STAMV) \tag{8}$$

Compute median of the matrix STAMV applying below detailed relation.

$$MV = median(STAMV) \tag{9}$$

Hybrid Stockwell index (HS-index) is computed by multiplication of VAI, VAV, MV and COVF using following relation.

$$HSindex = VAI \times VAV \times MV \times COVF \tag{10}$$

3) ALIENATION INDEX

Following relation is applied to compute correlation coefficient (CORC) of current samples i_1 and i_2 at an interval of quarter cycle.

$$CORC = \frac{N_s \sum i_1 i_2 - (\sum i_1)(\sum i_2)}{\sqrt{[N_s \sum i_1^2 - (\sum i_1)^2][N_s \sum i_2^2 - (\sum i_2)^2]}} \tag{11}$$

Here, Ns is the total samples in a cycle (Ns=64 are considered in this study); i_1: current sample at time t_0, i_2 current sample at time $-T + t_0$, T: time period of current waveform.

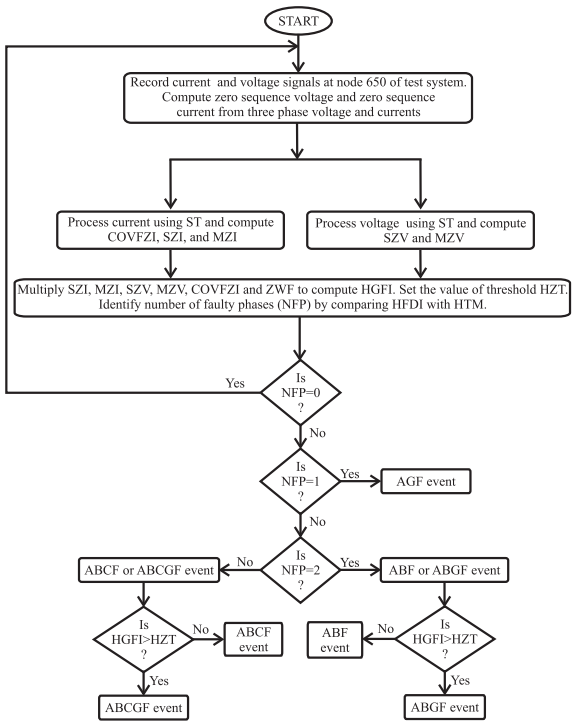

FIGURE 3. Fault classification algorithm.

The alienation index (A-index) is derived from CORC applying the below detailed relation.

$$Aindex = 1 - CORC^2 \tag{12}$$

4) HYBRID FAULT DETECTION INDEX

HFDI is evaluated by multiplication of HH-index, HS-index, A-index and a hybrid weight factor (HWF).

$$HFDI = HHindex \times Aindex \times HSindex \times HWF \tag{13}$$

Hybrid threshold magnitude (HTM) of 20000 is considered for HFDI to detect the fault events. This also discriminate the faults from healthy events. During faulty events, the magnitude HFDI is higher compared to the HTM and during the operational events this magnitude is lower compared to HTM.

B. FAULT EVENT CLASSIFICATION

Fault classification algorithm is described in Fig. 3. Fault events are classified and discriminated from each other using faulty phase numbers. To categorize the two phases fault and two phases to ground fault, a hybrid ground fault index (HGFI) is designed. HGFI also discriminates the three phase fault event with and without ground involvement. HGFI is computed by processing both the zero sequence voltage and current applying the ST. Following procedures is used to compute HGFI.

Calculate zero sequence current (I_0) using currents of all phases.

$$I_0 = \frac{(I_1 + I_2 + I_3)}{3} \tag{14}$$

Calculate zero sequence voltage (V_0) using voltages of all phases recorded on node 650 of test grid.

$$V_0 = \frac{(V_1 + V_2 + V_3)}{3} \tag{15}$$

Decompose zero sequence current using ST and obtain output matrix as detailed below.

$$STZI = \left(\int_{-\infty}^{+\infty} I_0 \frac{|f|}{\sqrt{2\pi}} e^{-\frac{f^2(\tau-t)^2}{2}} e^{-j2\pi ft} dt \right) \tag{16}$$

Decompose zero sequence voltage using ST and obtain output matrix as detailed below.

$$STZV = \left(\int_{-\infty}^{+\infty} V_0 \frac{|f|}{\sqrt{2\pi}} e^{-\frac{f^2(\tau-t)^2}{2}} e^{-j2\pi ft} dt \right) \tag{17}$$

Compute co-variance of summation of every column of STZI to compute zero sequence current co-variance factor (COVFZI).

$$COVFZI = cov(sum(STZI)) \tag{18}$$

Sum all the elements of a column of STZV matrix (SZI) as detailed below.

$$SZI = sum(STZI) \tag{19}$$

Sum all the elements of a column of STZV matrix (SZV) as detailed below.

$$SZV = sum(STZV) \tag{20}$$

Compute median of STZI (MZI) as detailed below.

$$MZI = median(STZI) \tag{21}$$

Compute median of STZV (MZV) as detailed below.

$$MZV = median(STZV) \tag{22}$$

Compute hybrid ground fault index by multiplication of MZI, MZV, SZI, SZV, COVFZI and weight factor (ZWF) as detailed below:-

$$HGFI = MZI \times MZV \times SZI \times SZV \times COVFZI \times ZWF \tag{23}$$

This study considered the Zero sequence weight factor (ZWF) qual to 10^6. A hybrid zero sequence threshold (HZT) equal to 50 is considered to investigate the ground involvement during the fault. Magnitude of HGFI higher than HZT identifies the ground involvement during fault. Magnitude of HGFI lower than HZT indicates that ground is not involved during fault event.

IV. DETECTION OF FAULTS: SIMULATION RESULTS

This section discussed the investigated fault events including phase-A to ground fault (AGF), phase-A and phase-B fault (ABF), phase-A and phase-B fault with involvement of ground (ABGF), three phase fault (ABCF), and three phase fault with ground (ABCGF).

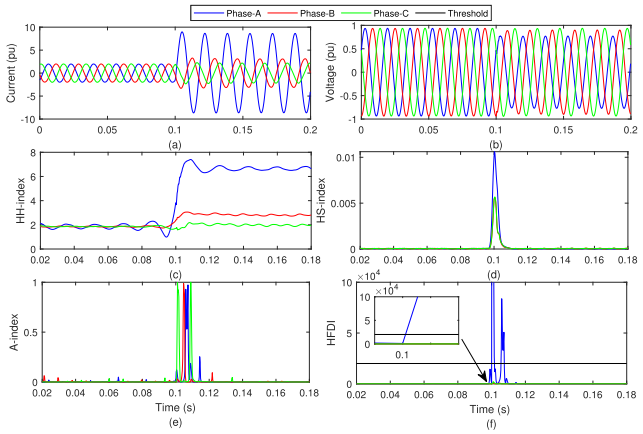

FIGURE 4. AGF event (a) current (b) voltage (c) HH-index (d) HS-index (e) A-index (f) HFDI.

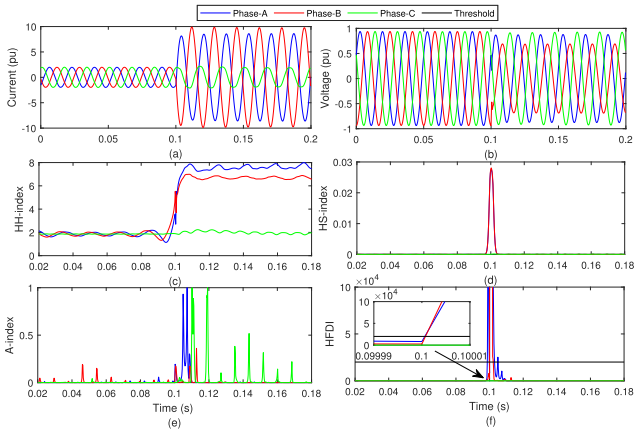

FIGURE 5. ABF event (a) current (b) voltage (c) HH-index (d) HS-index (e) A-index (f) HFDI.

A. AGF EVENT

An AGF event is incident on 671 node of test network at 6^{th} cycle. Current and voltage are measured on HPSL point of test system and detailed in Fig. 4 (a) and (b) respectively. These current and voltage are processed applying HT for computation of HH-index which is elaborated in Fig. 4 (c). Current and voltage are also processed using ST to computed HS-index which is shown in Fig. 4 (d). Current is processed using Alienation coefficient for computation of A-index which is detailed in Fig. 4 (e). Proposed HFDI is computed by multiplying the HH-index, HS-index, A-index and HWF which is illustrated in Fig. 4 (f). Time of fault detection and peak magnitude of HFDI for AGF event are included in Table 2.

Fig. 4 (a) indicates that current of fault phase-A is increased due to fault incidence at 6^{th} cycle. Fig. 4 (b) indicates that voltage of all phases decreased by small magnitude due to fault occurrence. However, decrease in magnitude of voltage of faulty Phase-A is more. Fig. 4 (c) indicates that HH-index magnitude of faulty phase-A increases due to fault occurrence at 6^{th} cycle. Further, magnitude of HH-index associated with healthy phases-A & B is increased slightly. Fig. 4 (d) indicates that HS-index magnitude of all phases has increased due to fault occurrence at 6^{th} cycle. Further, magnitude of faulty phase-A is more pronounced compared to healthy phases. Fig. 4 (e) indicates that A-index magnitude of all phases has increased to unity due to fault occurrence at 6^{th} cycle. Fig. 4 (f) indicates that HFDI magnitude of faulty phase is increased and becomes high in comparison to threshold. However, magnitude of healthy phases-B & C is low in comparison to threshold. Hence, AGF event has been effectively identified using the proposed algorithm. Table 2, indicates that AGF event is detected in small time interval of $1.1 \times 10^5 s$.

B. ABF EVENT

An ABF event between phases-A & B is incident on 671 node of test system at 6^{th} cycle. Current and voltage are measured on 650 node of test system and depicted in Fig. 5 (a) and (b) respectively. These current and voltage are processed using HT for computation of HH-index which is depicted in Fig. 5 (c). Current and voltage are also processed using ST for computation of HS-index which is shown in Fig. 5 (d). Current signal is processed using Alienation coefficient and A-index is computed which is detailed in Fig. 5 (e). Proposed HFDI is computed by multiplication of HH-index, HS-index, A-index and HWF which is illustrated in Fig. 5 (f). Time of fault detection and peak magnitude of HFDI of ABF event are included in Table 2.

Fig. 5 (a) indicates that current of fault phases-A & B is increased due to fault incidence at 6^{th} cycle. Fig. 5 (b) indicates that voltage of all phases decreased by small magnitude due to fault occurrence. However, decrease in magnitude of voltage of faulty phases-A & B is more. Fig. 5 (c) indicates that HH-index magnitude of fault phases-A & B has pronounced due to fault occurrence at 6^{th} cycle. Further, magnitude of HH-index corresponding to healthy phase-C is increased slightly. Fig. 5 (d) indicates that HS-index magnitude of fault phases-A & B has pronounced due to fault occurrence at 6^{th} cycle. However, magnitude of healthy phase-C increased by small amount compared to faulty phases. Fig. 5 (e) indicates that A-index magnitude of all phases has increased due to fault occurrence at 6^{th} cycle. Fig. 5 (f) indicates that HFDI magnitude of faulty phases-A & B is increased and becomes higher compared to threshold. However, magnitude of healthy phase-C is lower relative to threshold. Hence, AGF event is effectively identified using the proposed algorithm. Table 2, indicates that AGF event is detected in small time interval of $5 \times 10^6 s$.

C. ABGF EVENT

An ABGF event between phase-A and phase-B with ground involvement is incident on 671 node of test network at 6^{th} cycle. Current and voltage are measured on 650 node of test network and illustrated in Fig. 6 (a) and (b) respectively. These current and voltage are processed applying HT for computation of HH-index which is depicted in Fig. 6 (c).

TABLE 2. Peak magnitude of HFDI.

S.No.	Type of Fault	Fault estimation time (s)	Maximum Magnitude of HFDI		
			Phase-A	Phase-B	Phase-C
1	AGF	$1.1 \times 10^5 s$	6.1296×10^6	754.93	2115.5
2	ABF	$5 \times 10^6 s$	7.0068×10^6	8.3825×10^6	14.64
3	ABGF	$1 \times 10^6 s$	4.4933×10^6	2.2355×10^7	3814.5
4	ABCF	$1.5 \times 10^6 s$	4.1565×10^6	4.8473×10^7	1.8416×10^7
5	ABCGF	$1.5 \times 10^6 s$	4.2052×10^6	4.8975×10^7	2.1128×10^7

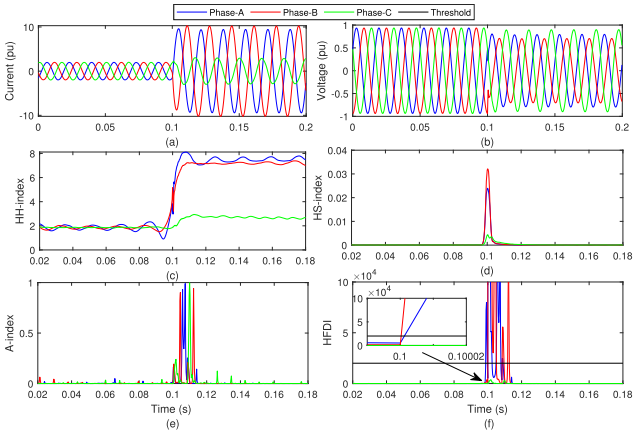

FIGURE 6. ABGF event (a) current (b) voltage (c) HH-index (d) HS-index (e) A-index (f) HFDI.

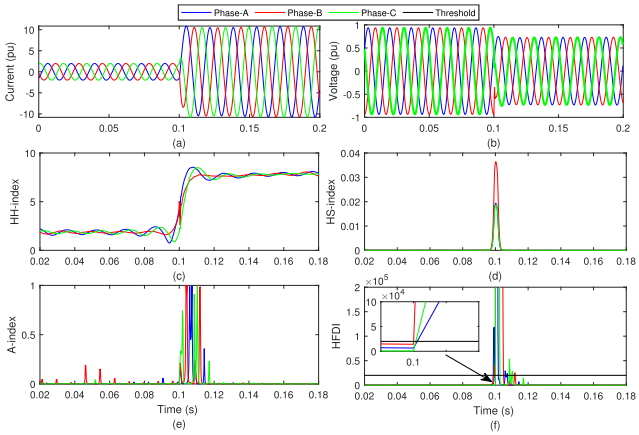

FIGURE 7. ABCF event (a) current (b) voltage (c) HH-index (d) HS-index (e) A-index (f) HFDI.

Current and voltage are also processed using ST to computed HS-index which is shown in Fig. 6 (d). Current is processed using Alienation coefficient for computation of A-index which is detailed in Fig. 6 (e). Proposed HFDI is computed by multiplication of HH-index, HS-index, A-index and HWF which is illustrated in Fig. 6 (f). Time of fault detection and peak magnitude of HFDI of ABGF event are included in Table 2.

Fig. 6 (a) indicates that current of faulty phases-A & B is increased due to ABGF event incidence at 6^{th} cycle. Fig. 6 (b) indicates that voltage of all phases decreased by small magnitude due to ABGF event occurrence. However, decrease in magnitude of voltage of faulty phases-A & B is more. Fig. 6 (c) indicates that HH-index magnitude of faulty phases-A & B has increased due to ABGF event occurrence at 6^{th} cycle. Further, magnitude of HH-index corresponding to healthy phase-C is increased slightly. Fig. 6 (d) indicates that HS-index magnitude of faulty phases-A & B has increased due to ABGF event occurrence at 6^{th} cycle. However, increase in magnitude of healthy phase-C is small compared to faulty phases. Fig. 6 (e) indicates that A-index magnitude of all phases has increased due to ABGF event occurrence at 6^{th} cycle. Fig. 6 (f) indicates that HFDI magnitude of faulty phases-A & B is increased and becomes high relative to to threshold. However, magnitude of healthy phase-C is lower relative to threshold. Hence, ABGF event is effectively identified using the proposed algorithm. Table 2, indicates that AGF event is detected in small time interval of $1.0 \times 10^6 s$.

D. ABCF EVENT

An ABCF event between all phases is incident on 671 node of test system at 6^{th} cycle. Current and voltage are measured on 650 node of test system and depicted in Fig. 7 (a) and (b) respectively. These current and voltage signals are processed using HT for computation of HH-index which is elaborated in Fig. 7 (c). Current and voltage are also processed using ST for computation of HS-index which is shown in Fig. 7 (d). Current is processed using Alienation coefficient and A-index is computed which is detailed in Fig. 7 (e). Proposed HFDI is computed by multiplication of HH-index, HS-index, A-index and HWF which is illustrated in Fig. 7 (f). Time of fault detection and peak magnitude of HFDI of ABCF event are included in Table 2.

Fig. 7 (a) indicates that current of all phases is increased due to ABCF event incidence at 6^{th} cycle. Fig. 7 (b) indicates that voltage of all phases decreased by small magnitude due to ABCF event occurrence. Fig. 7 (c) indicates that HH-index magnitude of all phases has increased due to ABCF event occurrence at 6^{th} cycle. Fig. 7 (d) indicates that HS-index magnitude of all phases has increased due to ABCF event occurrence at 6^{th} cycle. Fig. 7 (e) indicates that A-index magnitude of all phases has increased due to ABCF event occurrence at 6^{th} cycle. Fig. 7 (f) indicates that HFDI magnitude of all phases is increased and becomes high relative to threshold. Hence, ABCF event is effectively identified using the proposed algorithm. Table 2, indicates that AGF event is detected in small time interval of $1.5 \times 10^6 s$.

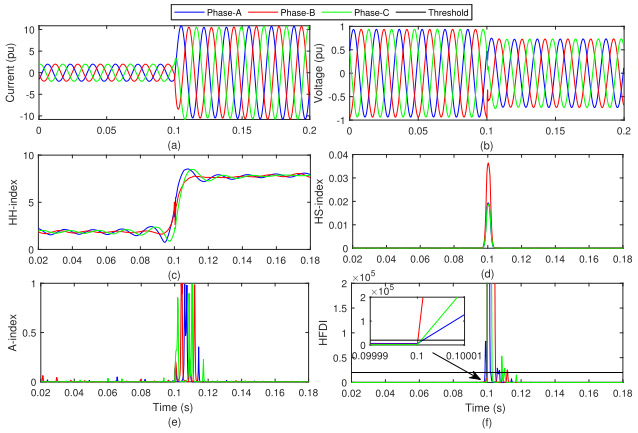

FIGURE 8. ABCGF event (a) current (b) voltage (c) HH-index (d) HS-index (e) A-index (f) HFDI.

E. ABCGF EVENT

An ABCGF event between all phases with involvement of ground is incident on 671 node of test system at 6^{th} cycle. Current and voltage are measured on 650 node of test system and depicted in Fig. 8 (a) and (b) respectively. These current and voltage are processed using HT for computation of HH-index which is depicted in Fig. 8 (c). Current and voltage are also processed applying ST for computation of HS-index which is shown in Fig. 8 (d). Current is processed using Alienation coefficient and A-index is computed which is detailed in Fig. 8 (e). Proposed HFDI is computed by multiplication of HH-index, HS-index, A-index and HWF which is illustrated in Fig. 8 (f). Time of fault detection and peak magnitude of HFDI of ABCGF event are included in Table 2.

Fig. 8 (a) indicates that current of all phases is increased due to ABCGF event incidence at 6^{th} cycle. Fig. 8 (b) indicates that voltage of all phases decreased by small magnitude due to ABCGF event occurrence. Fig. 8 (c) indicates that HH-index magnitude of all phases has increased due to ABCGF event occurrence at 6^{th} cycle. Fig. 8 (d) indicates that HS-index magnitude of all phases has increased due to ABCGF event occurrence at 6^{th} cycle. Fig. 8 (e) indicates that A-index magnitude of all phases has increased due to ABCGF event occurrence at 6^{th} cycle. Fig. 8 (f) indicates that HFDI magnitude of all phases is increased and becomes high relative to threshold. Hence, ABCGF event has been effectively identified using the proposed algorithm. Table 2, indicates that AGF event is detected in small time interval of $1.5 \times 10^6 s$.

F. FAULT CLASSIFICATION

Faults are categorized using faulty phase numbers. One phase and ground fault (AG, BG, CG) event is identified when HFDI is greater than threshold for one phase only. Two phase fault event with and without ground involvement (AB, BC, AC, ABG, BCG, ACG) is identified when HFDI is high relative to threshold for two phases. Ground involvement during two phase fault event is identified using HGFI as illustrated in Fig. 9. Magnitude of HGFI greater than hybrid zero sequence threshold (HZT) indicates that ground is fault part during the event of fault and ABG fault is discriminated from the AB fault event. Three phase fault event with and without ground involvement (ABC, ABCG) is identified when HFDI is greater than threshold for all three phases. Ground involvement during three phase fault is recognized using HGFI. Magnitude of HGFI will be greater than HZT due to ground involvement during three phase fault.

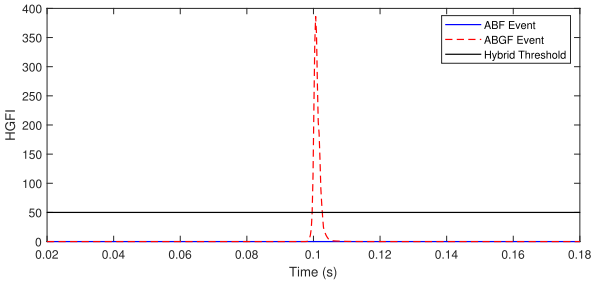

FIGURE 9. HGFI to identify ground involvement during two phase faults.

V. SIMULATION RESULTS: CASE STUDIES

Proposed protection algorithm is tested for different case studies to generalize the application and functionality for different scenario of grid.

A. FAULT INCIDENCE ANGLE VARIATIONS

An AGF event is incident on 671 node of test network at 6^{th} cycle for angle of fault incidence angles (AFI) of 0°, 30°, 45°, 60°, 90°, 120°, 150° and 180° to test functionality of protection algorithm for different angles of current and voltage waveform. Current and voltage are measured on HPSL point of test grid are processed applying protection algorithm to compute the HFDI. Peak magnitudes of HFDI corresponding to all investigated AFI is included in Table 3.

This has been observed from Table 3 that maximum value of HFDI for faulty phase-A has become high relative to threshold of 20000 corresponding to all investigated AFIs. The peak magnitude of HFDI for healthy phases-A & B is lower than threshold magnitude of 20000 corresponding to all investigated AFIs. Therefore, it is established that protection scheme functions effectively to detect fault events incident at different AFI on the voltage and current waveform.

B. FAULT IMPEDANCE VARIATIONS

An AGF event is simulated on node 671 of test utility grid at 6^{th} cycle taking fault impedance of 0.01Ω, 2Ω, 4Ω, 6Ω, 8Ω, and 10Ω to test functionality of protection algorithm for different fault impedance. Current and voltage are recorded on node 650 of test network are processed using protection

TABLE 3. Maximum value of HFDI during AGF event for different fault incidence angle.

S.No.	Phase	Peak Magnitude of HFDI							
		0°	30°	45°	60°	90°	120°	150°	180°
1	A	6.1296×10^5	1.0794×10^6	2.9×10^6	2.0079×10^6	1.7322×10^6	1.3414×10^6	1.0458×10^5	5.7171×10^5
1	B	754.93	935.32	1087.7	5419.8	2342	663.09	92.488	707.21
1	C	2115.5	902.98	2163.9	4204	562.51	153.09	39.975	2009.7

algorithm to compute the HFDI. Peak magnitudes of HFDI corresponding to all investigated fault impedance is provided in Table 4.

Table 4 indicates that maximum magnitude of HFDI for faulty phase-A has become high relative to threshold of 20000 corresponding to all investigated fault impedance. The peak magnitude of HFDI for healthy phases-A & B is lower than threshold of 20000 corresponding to all investigated fault impedance. Therefore, proposed protection algorithm functions effectively for detecting the fault events incident on voltage and current waveform with different fault impedance.

C. AGF EVENT INCIDENT AT DIFFERENT TEST NODES

An AGF event is incident on different nodes of test grid at 6^{th} cycle to test functionality of protection algorithm for different fault incidence nodes. Current and voltage are captured on 650 node of test grid are processed using protection algorithm to compute HFDI. Peak magnitudes of HFDI corresponding to all investigated fault incidence nodes is included in Table 5.

Table 5 indicates that maximum magnitude of HFDI for faulty phase-A has become high relative to threshold of 20000 corresponding to all investigated fault incidence nodes. Peak magnitude of HFDI for healthy phases-A & B is lower than threshold of 20000 corresponding to all investigated fault incidence nodes. Therefore, it is established that protection algorithm functions effectively to detect fault events incident on different incidence nodes.

D. EFFECT OF NOISE

An AGF event is incident on 671 node of test grid at 6^{th} cycle. Current and voltage are recorded on 650 node of test grid. A noise of $20dB$ SNR is superimposed on both the current and voltage and illustrated in Fig. 10 (a) and (b) respectively. These noisy current and voltage are processed applying HT for computation of HH-index which is depicted in Fig. 10 (c). The noisy current and voltage are also processed applying ST to compute HS-index which is shown in Fig. 10 (d). Noisy current is processed using Alienation coefficient and A-index is computed which is detailed in Fig. 10 (e). Proposed HFDI is computed by multiplication of HH-index, HS-index, A-index and HWF which is depicted in Fig. 10 (f).

Fig. 10 (a) details that current of faulty phase-A is pronounced due to fault incident at 6^{th} cycle. Fig. 10 (b) elaborates that voltage of all phases decreased by small magnitude due to fault occurrence. However, decrease in magnitude of voltage of faulty Phase-A is more. Fig. 10 (c) indicates that HH-index magnitude of faulty phase-A has pronounced

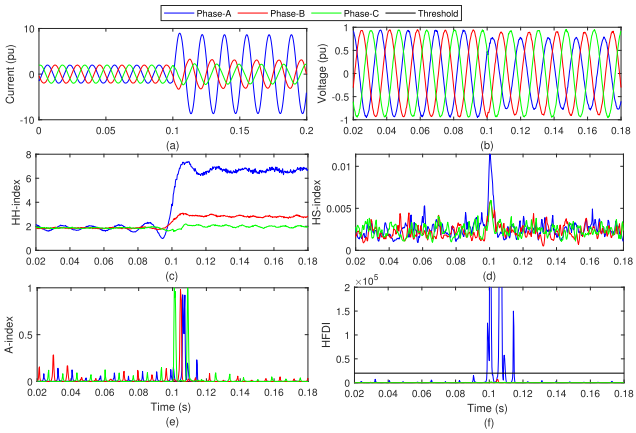

FIGURE 10. AG fault in noisy condition (a) current (b) voltage (c) HH-index (d) HS-index (e) A-index (f) HFDI.

due to fault occurrence at 6^{th} cycle. Further, magnitude of HH-index associated with healthy phases-A & B is increased slightly. Fig. 10 (d) indicates that HS-index magnitude of all phases has increased due to fault occurrence at 6^{th} cycle. However, magnitude of faulty phase-A is more pronounced compared to healthy phases. Additionally, high magnitude spikes are also observed due to noise presence over entire time range. Fig. 10 (e) indicates that A-index magnitude of all phases has increased to unity due to fault occurrence at 6^{th} cycle. Small magnitude spikes are observed due to noise over complete time range. Fig. 10 (f) indicates that HFDI magnitude of faulty phase is increased and becomes high relative to threshold. Further, magnitude of healthy phases-B & C is lower relative to threshold. Hence, AGF event is effectively identified in noisy environment using the proposed algorithm.

VI. BEHAVIOR OF PROTECTION SCHEME WITH OPERATIONAL EVENTS

Simulation results for discriminating the faulty events from operational events are discussed in this section.

A. LOAD OPERATION

A load of $843kW$ and $462kVAr$ connected on 675 node of test network is switched off at 4^{th} cycle and reconnected to grid at 8^{th} cycle. Current and voltage are measured on 650 node of test network and illustrated in Fig. 11 (a) and (b) respectively. These current and voltage are processed applying the HT and HH-index is derived which is depicted in Fig. 11 (c). Current and voltage are also processed using ST to computed HS-index which is shown in Fig. 11 (d). Current is processed using Alienation coefficient and A-index is derived which is

TABLE 4. Maximum value of HFDI during AGF event for fault impedance variation.

S.No.	Phase	Peak Magnitude of HFDI					
		0.01Ω	2Ω	4Ω	6Ω	8Ω	10Ω
1	A	6.1296×10^5	3.4626×10^5	2.058×10^5	1.2953×10^5	84544	57061
2	B	754.93	459.17	288.95	246.05	214.13	177.1
3	C	2115.5	1050.7	636.5	451.46	376.14	321.63

TABLE 5. Maximum value of HFDI during AGF event at different nodes of test utility grid.

S.No.	Phase	Peak Magnitude of HFDI					
		671	675	652	611	646	634
1	A	6.1296×10^5	8.0159×10^5	4.2192×10^5	1.8139×10^5	7.9263×10^5	2.1338×10^6
2	B	754.93	2188.6	2352.5	1102.6	343.75	458.11
3	C	2115.5	1058.6	706.19	2431.6	305.07	494.46

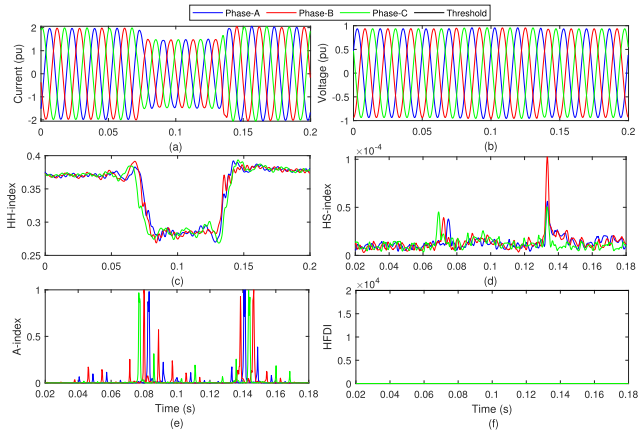

FIGURE 11. Load operation (a) current (b) voltage (c) HH-index (d) HS-index (e) A-index (f) HFDI.

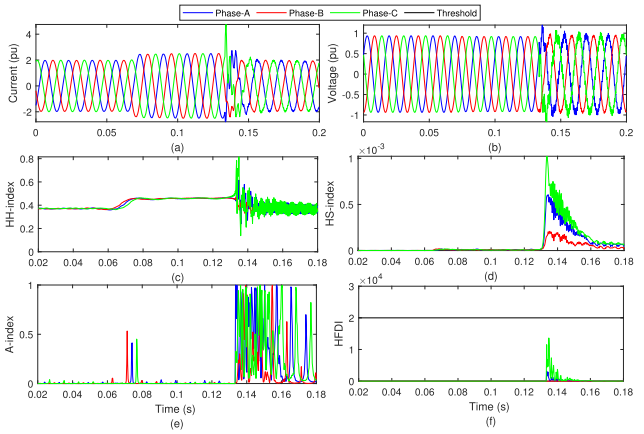

FIGURE 12. Capacitor operation (a) current (b) voltage (c) HH-index (d) HS-index (e) A-index (f) HFDI.

detailed in Fig. 11 (e). Proposed HFDI is computed by multiplying the HH-index, HS-index, A-index and HWF which is illustrated in Fig. 11 (f).

Fig. 11 (a) indicates that current of all phases has decreased between 4^{th} cycle to 8^{th} cycle. Fig. 11 (b) indicates that voltage of all phases remains unaffected. Fig. 11 (c) details that HH-index magnitude of all phases has decreased between 4^{th} cycle to 8^{th} cycle. Fig. 11 (d) indicates that HS-index magnitude of all phases has high magnitude peaks at 4^{th} cycle to 8^{th} cycle. Further, magnitude of peak at 8^{th} cycle is relatively high. Fig. 11 (e) indicates that A-index magnitude of all phases has peaks of unit magnitude at 4^{th} cycle and 8^{th} cycle. Fig. 11 (f) indicates that HFDI magnitude of all phases is lower relative to threshold. Hence, load operation event is considered as non-faulty event and differentiated from faulty events effectively using the proposed algorithm.

B. CAPACITOR OPERATION

A capacitor rated at $600kVAr$ connected on 675 node of test system is switched off at 4^{th} cycle and reconnected to grid at 8^{th} cycle. Current and voltage are measured on HPSL point of test grid and illustrated in Fig. 12 (a) and (b) respectively. These current and voltage are processed applying the HT and HH-index is derived which is depicted in Fig. 12 (c). The current and voltage are also processed using ST to computed HS-index which is shown in Fig. 12 (d). Current is processed using Alienation coefficient and A-index is derived which is detailed in Fig. 12 (e). Proposed HFDI is computed by multiplying the HH-index, HS-index, A-index and HWF which is illustrated in Fig. 12 (f).

Fig. 12 (a) indicates that current of all phases has increased between 4^{th} cycle to 8^{th} cycle. A current spike is also incident at capacitor switching on instant. Fig. 12 (b) indicates that voltage magnitude of all phases remains same but low magnitude voltage spikes are observed due to switching on the capacitor at 8^{th} cycle. Fig. 12 (c) indicates that HH-index magnitude of all phases has increased between 4^{th} cycle to 8^{th} cycle. Fig. 12 (d) indicates that HS-index magnitude of all phases has high magnitude peaks at 4^{th} cycle to 8^{th} cycle. Further, magnitude of peaks at 8^{th} cycle is relatively high. Fig. 12 (e) indicates that A-index magnitude of all phases has peaks of high magnitude at 4^{th} cycle and 8^{th} cycle. Fig. 12 (f) indicates that HFDI of all phases is low relative to threshold at instant of switching on and off the capacitor. Hence, load operation event is considered as non-faulty event and differentiated from fault events effectively using the proposed algorithm.

TABLE 6. Details of DTs and loads connected to practical distribution feeders.

S. No.	Symbol of DT	kVA rating of DT	Symbol of Load	Quantity of Load (kW)
1	ADT-1	63kVA, 11/0.44kV	AL-1	$41kW$
2	ADT-2	160kVA, 11/0.44kV	AL-2	$119kW$
3	ADT-3	40kVA, 11/0.44kV	AL-3	$28kW$
4	ADT-4	10kVA, 11/0.44kV	AL-4	$5kW$
5	ADT-5	16kVA, 11/0.44kV	AL-5	$9kW$
6	BDT-1	160kVA, 11/0.44kV	BL-1	$111kW$
7	BDT-2	100kVA, 11/0.44kV	BL-2	$72kW$
8	BDT-3	16kVA, 11/0.44kV	BL-3	$12kW$
9	CDT-1	100kVA, 11/0.44kV	CL-1	$64kW$
10	CDT-2	25kVA, 11/0.44kV	CL-2	$17kW$
11	CDT-3	10kVA, 11/0.44kV	CL-3	$4kW$
12	CDT-4	25kVA, 11/0.44kV	CL-4	$21kW$
13	SST	13MVA, 33/11kV	-	-

TABLE 7. Details of SPPs, WPP and transformers.

S. No.	Symbol of SPP/WPP	Bus on which SPP/ WPP connected	Capacity of SPP/WPP (kW)	Symbol of transformer	Rating of transformer
1	SPP-1	B-4	$50kW$	ST-1	63 kVA, 0.220/11kV
2	SPP-2	B-6	$80kW$	ST-2	100 kVA, 0.220/11kV
3	SPP-3	B-9	$40kW$	ST-3	50 kVA, 0.220/11kV
4	SPP-4	B-10	$20kW$	ST-4	25 kVA, 0.220/11kV
5	WPP-1	B-13	$100kW$	WT-1	160 kVA, 0.690/11kV

TABLE 8. Comparative analysis.

Description	Reference [19]	Proposed Algorithm
Sampling frequency (kHz)	-	3.84
Fault classification	Examined	Examined
Noise effect	Not examined	Examined
Noise effect on performance	Deteriorated at $40dB$ SNR	Effective upto $20dB$ SNR
Operational events	Not examined	Examined
Fault impedance variation	Examined	Examined
Angle of fault incidence variation	Examined	Examined

C. FEEDER OPERATION

Test grid feeder of 692 and 675 nodes is tripped at 4^{th} cycle and charged again at 8^{th} cycle. Current and voltage are measured on 650 node of test grid and depicted in Fig. 13 (a) and (b) respectively. These current and voltage are processed using HT and HH-index is derived which is depicted in Fig. 13 (c). Current and voltage are also processed using ST to computed HS-index which is shown in Fig. 13 (d). Current is processed using Alienation coefficient and A-index is derived which is detailed in Fig. 13 (e). Proposed HFDI is computed by multiplication of HH-index, HS-index, A-index and HWF which is depicted in Fig. 13 (f).

Fig. 13 (a) indicates that current of all phases has remains un-affected between 4^{th} cycle to 8^{th} cycle. High magnitude current spikes are observed at moment of feeder re-closing. Fig. 13 (b) indicates that voltage magnitude of all phases remains same but low magnitude voltage spikes are observed due to switching on the feeder at 8^{th} cycle. Fig. 13 (c) indicates that HH-index magnitude of all phases remains same. However, high magnitude oscillations are observed due to feeder re-closing after 8^{th} cycle. Fig. 13 (d) indicates that HS-index magnitude of all phases has high magnitude peaks at 4^{th} cycle and 8^{th} cycle. Further, magnitude of peaks at 8^{th} cycle is relatively high. Fig. 13 (e) indicates that A-index magnitude of all phases has peaks of high magnitude at 4^{th} cycle and 8^{th} cycle. Fig. 13 (f) indicates that HFDI of all phases is lower relative to threshold at feeder tripping and re-closing instants. Hence, load operation event is considered

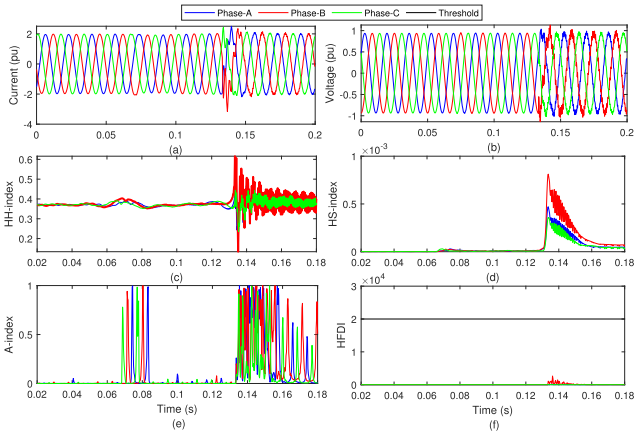

FIGURE 13. Feeder operation (a) current (b) voltage (c) HH-index (d) HS-index (e) A-index (f) HFDI.

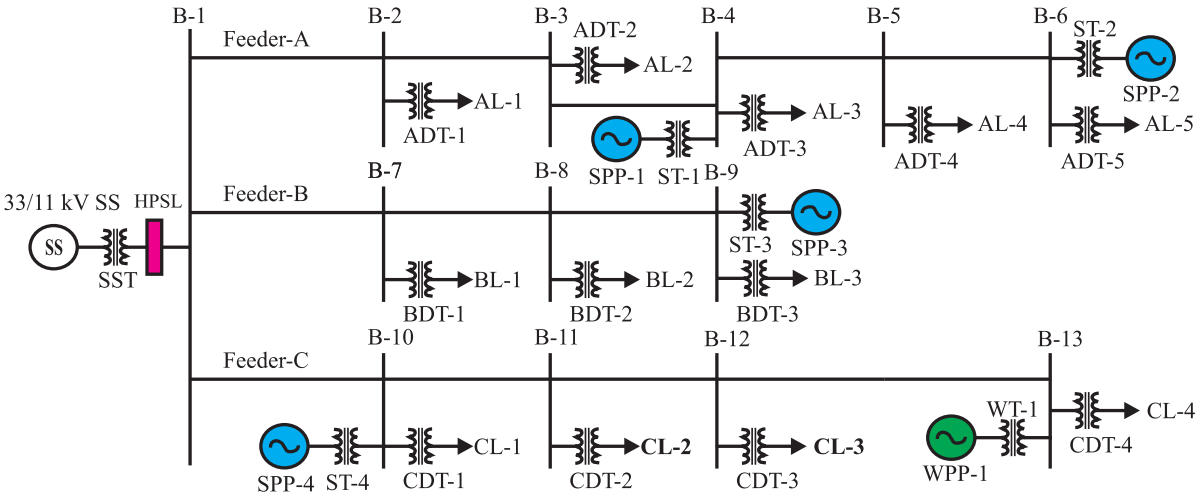

FIGURE 14. Practical distribution network.

as non-faulty event and differentiated from faulty events effectively using the proposed algorithm.

VII. TESTING OF PROTECTION SCHEME ON PRACTICAL UTILITY GRID

Distribution network of a practical utility grid rated at 11 kV is considered to validate performance of proposed protection schemes in real time scenario which is detailed in Fig. 14. This distribution network is fed from the 33/11 kV sub-station (SS) of sub-transmission system. Sub-station transformer is rated at 13 MVA, 33/11 kV. Bus B-1 is operated at 11 kV from where three feeders (Feeder-A, Feeder-B & Feeder-C) are emanating which feed the load in the a Phalodi region of India. Loads fed by distribution transformers (DT) are represented as concentrated load on the DT. All DTs are rated as 11/0.44kV. Five distribution transformers represented as ADT-1 to ADT-5 are connected to Feeder-A. Loads connected to these DTs are represented as AL-1 to AL-5 respectively. Three distribution transformers represented as BDT-1 to BDT-3 are connected to Feeder-B. Loads connected to these DTs are represented as BL-1 to BL-3 respectively. Four distribution transformers represented as CDT-1 to CDT-4 are connected to Feeder-C. Loads connected to these DTs are represented as CL-1 to CL-4 respectively. Details of loads and DTs is included in Table 6. All feeders use the aluminum conductor steel reinforced (ACSR) Weasal conductor rated at 11 kV having current carrying capacity of 114*A* [18]. Four solar power plants (SPP) designated as SPP-1 to SPP-2 are connected to the feeders using solar transformers (ST) ST-1 to ST-4 respectively. One wind power plant (WPP) is also connected to node B-13 using Wind transformer (WT-1). Details of SPPs and WPP with their transformers are included in Table 7. Incomer of 33/11kV transformer on the bus B-1 is considered as the HPSL for data measurement.

Fault data are recorded from the disturbance recorder installed at the 33/11kV Sub-station. Data of voltage and current corresponding to an AGF event incident on the node B-5 of test feeder-A are processed applying the proposed protection algorithm and HFDI is derived which is illustrated in Fig. 15. Peak HFDI associated to phases-A, B & C are computed as 3.3868×10^6, 8910.8, and 11264 respectively. It is inferred that peak of HFDI for faulty phase-A is high relative to threshold HTM and it is low relative to healthy phases-B & C. Hence, AGF event observed on a real time distribution network is detected effectively.

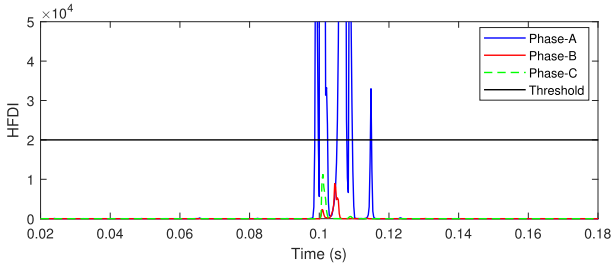

FIGURE 15. HFDI during an AGF event incident on a feeder of practical utility grid.

VIII. PERFORMANCE COMPARATIVE ANALYSIS

To generalize the proposed protection approach, performance of algorithm is compared with alienation based protection algorithm reported in [19]. Comparative analysis of alienation based protection schemes and proposed approach considering different case studies and parameters is described Table 8. Investigated cases are indicated by *Examined* and cases which are not considered are indicated as *Not examined*. It is concluded that proposed protection schemes is more generalized compared to the algorithm introduced in [19]. Further, performance of alienation based method is affected for high noise levels and effective upto noise level of 40*dB* SNR. However, algorithm considered in this paper works well for noise levels of 20*dB* SNR. Further, proposed approach is

more generalized for utility grids operating at high renewable energy share.

IX. CONCLUSION

A protection schemes for utility grid with high penetration of RE generation based on feature computed from voltage and current signals using HT, ST, and Alienation coefficient to detect fault events with the help of HFDI is presented in this paper. Fault classification is achieved using faulty phase numbers and a HGFI. It is concluded that protection schemes effectively detect fault events such as AGF, ABF, ABGF, ABCF, and ABCGF incident on a utility grid of IEEE-13 bus test system with 50% RE penetration. Algorithm is effective to detect faults incident at different nodes of test grid, different fault impedance, and different angles of fault incidence. Protection scheme is effective to detect faults with high noise levels of 20*dB* SNR. Protection scheme is effective to discriminate the operational events from the faulty ones. This is also concluded that protection scheme effectively detects the faults incident on a practical distribution network with RE penetration of 57%. This is also concluded that protection scheme is better relative to Alienation coefficient based protection scheme reported in literature.

REFERENCES

[1] T. Ahmad and D. Zhang, "Renewable energy integration/techno-economic feasibility analysis, cost/benefit impact on islanded and grid-connected operations: A case study," *Renew. Energy*, vol. 180, pp. 83–108, Dec. 2021.
[2] A. Chandra, G. K. Singh, and V. Pant, "Protection of AC microgrid integrated with renewable energy sources—A research review and future trends," *Electr. Power Syst. Res.*, vol. 193, Apr. 2021, Art. no. 107036.
[3] M. Shaik, A. G. Shaik, and S. K. Yadav, "Hilbert–Huang transform and decision tree based islanding and fault recognition in renewable energy penetrated distribution system," *Sustain. Energy, Grids Netw.*, vol. 30, Jun. 2022, Art. no. 100606.
[4] A. Srivastava and S. K. Parida, "Data driven approach for fault detection and Gaussian process regression based location prognosis in smart AC microgrid," *Electr. Power Syst. Res.*, vol. 208, Jul. 2022, Art. no. 107889.
[5] P. Mohammadi, H. El-Kishyky, M. Abdel-Akher, and M. Abdel-Salam, "The impacts of distributed generation on fault detection and voltage profile in power distribution networks," in *Proc. IEEE Int. Power Modulator High Voltage Conf. (IPMHVC)*, Jun. 2014, pp. 191–196.
[6] B. Patnaik, M. Mishra, R. C. Bansal, and R. K. Jena, "MODWT-XGBoost based smart energy solution for fault detection and classification in a smart microgrid," *Appl. Energy*, vol. 285, Mar. 2021, Art. no. 116457.
[7] H. H. Alhelou, M. E. H. Golshan, and J. Askari-Marnani, "Robust sensor fault detection and isolation scheme for interconnected smart power systems in presence of RER and EVs using unknown input observer," *Int. J. Electr. Power Energy Syst.*, vol. 99, pp. 682–694, Jul. 2018.
[8] A. K. Soni and A. Yadav, "Fault detection and classification of grid connected wind farm (DFIG) using fuzzy logic controller," in *Proc. IEEE Int. Power Renew. Energy Conf. (IPRECON)*, Sep. 2021, pp. 1–6.
[9] M. Eslami, M. Jannati, and S. S. Tabatabaei, "An improved protection strategy based on PCC-SVM algorithm for identification of high impedance arcing fault in smart microgrids in the presence of distributed generation," *Measurement*, vol. 175, Apr. 2021, Art. no. 109149.
[10] J. O. C. P. Pinto and M. Moreto, "Protection strategy for fault detection in inverter-dominated low voltage AC microgrid," *Electr. Power Syst. Res.*, vol. 190, Jan. 2021, Art. no. 106572.
[11] W. H. Kersting, "Radial distribution test feeders," *IEEE Trans. Power Syst.*, vol. 6, no. 3, pp. 975–985, Aug. 1991.
[12] O. P. Mahela and A. G. Shaik, "Power quality recognition in distribution system with solar energy penetration using S-transform and fuzzy C-means clustering," *Renew. Energy*, vol. 106, pp. 37–51, Jun. 2017.
[13] O. P. Mahela and A. G. Shaik, "Power quality detection in distribution system with wind energy penetration using discrete wavelet transform," in *Proc. 2nd Int. Conf. Adv. Comput. Commun. Eng.*, May 2015, pp. 328–333.
[14] A. G. Shaik and O. P. Mahela, "Power quality assessment and event detection in hybrid power system," *Electr. Power Syst. Res.*, vol. 161, pp. 26–44, Mar. 2018.
[15] A. Derviskadic, G. Frigo, and M. Paolone, "Beyond phasors: Modeling of power system signals using the Hilbert transform," *IEEE Trans. Power Syst.*, vol. 35, no. 4, pp. 2971–2980, Jul. 2019.
[16] O. P. Mahela, A. G. Shaik, B. Khan, R. Mahla, and H. H. Alhelou, "Recognition of complex power quality disturbances using S-transform based ruled decision tree," *IEEE Access*, vol. 8, pp. 173530–173547, 2020.
[17] P. Ghasemzadeh, H. Kalbkhani, and M. G. Shayesteh, "Sleep stages classification from EEG signal based on stockwell transform," *IET Signal Process.*, vol. 13, no. 2, pp. 242–252, Apr. 2019.
[18] J. S. Saini, M. Sharma, and S. Singh, "Voltage profile improvement of rural distribution network by conductor replacement," *Int. Electr. Eng. J.*, vol. 5, no. 7, pp. 1490–1494, 2014.
[19] B. Rathore and A. G. Shaik, "Alienation based fault detection and classification in transmission lines," in *Proc. Annu. IEEE India Conf. (INDICON)*, Dec. 2015, pp. 1–6.

ABHISHEK GUPTA received the Bachelor of Engineering degree (Hons.) in electrical engineering from the Ajmer Institute of Technology, Ajmer, affiliated to University of Rajasthan, Jaipur, India, in 2009, and the Master of Technology degree in power systems from the Marudhar Engineering College, Bikaner, affiliated to RTU, Kota, India, in 2014. He is currently pursuing the Ph.D. degree in power systems with the Swami Keshvanand Institute of Technology Management and Gramothan, Jaipur, affiliated to RTU, Kota. He is currently working as a Faculty Member with the Department of Electrical Engineering, Swami Keshvanand Institute of Technology Management and Gramothan, Jaipur. His research interests include signal processing technique, grid integration of renewable energy, and power system protection. He always excelled in academics and awarded the Gold Medal at Graduate level. He was a recipient of the Best Paper Award from 4th IEEE International Conference on Electrical, Computer and Electronics (UPCON–2017).

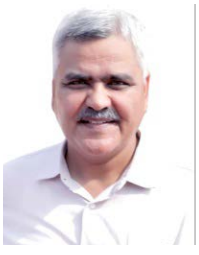

RAMESH KUMAR PACHAR received the Bachelor of Engineering degree in electrical and electronics engineering from Karnataka University, Dharwad, India, in 1998, and the Master of Technology and Doctor of Philosophy degrees in power system engineering from the Malviya National Institute of Technology, Jaipur, India, in 2005 and 2012, respectively. He is currently working as a Principal with the Swami Keshvanand Institute of Technology Management and Gramothan, Jaipur. He was a recipient of Best Teacher Award. He has more than 22 years of teaching and research experience. He has authored many research articles in reputed national and international journals and conferences. His research interests include power quality issues, smart grid technologies, power electronics, power system network reconfiguration, power quality analysis, and renewable energy integration.

OM PRAKASH MAHELA (Senior Member, IEEE) received the B.E. degree in electrical engineering from the College of Technology and Engineering, Udaipur, India, in 2002, the M.Tech. degree in electrical engineering from Jagannath University, Jaipur, India, in 2013, the Ph.D. degree in electrical engineering from IIT Jodhpur, India, in 2018, and the M.B.A. degree in human resource management from Indira Gandhi National Open University, New Delhi, India, in 2021. From 2002 to 2004, he was an Assistant Professor at the Rajasthan Institute of Engineering and Technology, Jaipur. From 2004 to 2014, he was a Junior Engineer at Rajasthan Rajya Vidyut Prasaran Nigam Ltd., India, and an Assistant Engineer, since February 2014. He has authored more than 240 research articles and book chapters. He has edited five books. He performed more than 290 reviews for the prestigious journals of IEEE, Elsevier, Springer, Willey, and Taylor & Francis. His research interests include power quality, power system planning, grid integration of renewable energy sources, FACTS devices, transmission line protection, and condition monitoring. He was a recipient of the University Rank Certificate, in 2002; the Gold Medal, in 2013; the Best Research Paper Award, in 2018; the C. V. Raman Gold Medal, in 2019; and the Senior Professional Engineer Award, in 2021. He has been included in top 2% Scientists worldwide, in 2021 and 2022. He received the certificates of outstanding contribution in the reviewing from *Computer and Electrical Engineering*, the *International Journal of Electrical Power and Energy Systems*, *Measurement*, and *Renewable and Sustainable Energy Reviews*.

BASEEM KHAN (Senior Member, IEEE) received the Bachelor of Engineering degree in electrical engineering from Rajiv Gandhi Technological University, Bhopal, India, in 2008, and the Master of Technology and Doctor of Philosophy degrees in electrical engineering from the Maulana Azad National Institute of Technology, Bhopal, in 2010 and 2014, respectively. He is currently working as a Faculty Member with Hawassa University, Ethiopia. His research interests include power system restructuring, power system planning, smart grid technologies, meta-heuristic optimization techniques, reliability analysis of renewable energy systems, power quality analysis, and renewable energy integration.